AIAA JOURNAL
Vol. 30, No. 6, June 1992

# Navier-Stokes Simulation for Cone-Derived Waverider

Jiun-Rong Liao* and Kakkattukuzhy M. Isaac†
*University of Missouri—Rolla, Rolla, Missouri 65401*
and
John B. Miles‡ and Bor-Jang Tsai*
*University of Missouri—Columbia, Columbia, Missouri 65211*

**The three-dimensional, laminar flowfield associated with conical waveriders, whose cross-plane lower surface is derived from an ellipse, has been analyzed in the present study by numerical simulation of the Navier-Stokes equations. The numerical method uses the flux difference splitting algorithm. Both Euler and viscous solutions have been obtained. Results of zero angle-of-attack and 5-deg angle-of-attack cases, respectively, are presented. The analysis to date has dealt with the forebody only. Surface pressure coefficients are compared with experimental data. Skin friction coefficients are calculated and lift and drag values are estimated. The skin friction, lift, and drag values are compared with previous analytic estimates and they are found to be in reasonably good agreement. The study provides valuable preliminary insight into the feasibility of using waverider configurations for aircraft design.**

## I. Introduction

WAVERIDERS, one application of classical gas dynamics, come from early re-entry vehicle design. In recent years, investigators have shown renewed interest in them with increased focus on the National Aerospace Plane project, which requires blended design with wing-body-tail-inlet-engine integration. Mass capture and optimum effective specific impulse are other important requirements.

Any supersonic manned vehicle or guided missile that is maneuverable and has the requirement of cruise range has a propulsion system that provides thrust. If the amount of aerodynamic lift in level flight is sufficient to overcome the gravitational force, then the thrust of the propulsion system is necessary only to overcome the drag. Therefore, the engineer's desire is for such vehicles to have high lift and low drag and reasonable structural efficiency, and to provide useful internal storage space. A class of high lift vehicles, resulting from the lifting pressure of the entire lower surface at relatively higher values than that of the top surface,[1,2] called waveriders, has been studied since the 1950s. In order to speed up the design process, approximate solutions rather than exact solutions have often been used. Maikapar[3] was one of the first who employed an approximate flowfield about circular cones at zero angle of attack to generate waverider shapes. He obtained a simple formula for the streamline through any given point in the flowfield about a cone, which could allow one to quickly construct bodies from intersecting conical flowfields. Many other approximate treatments of conical flows (see Refs. 4–6) have been developed. Any of these, or other approximate methods, can be exploited to determine the flowfields from which waverider configurations can be developed. The most advanced of these procedures is the perturbation analysis described by Jischke.[4] This procedure is based on a flow perturbation about either a circular cone or an elliptic cone developed by Doty and Rasmussen.[5] The general cross-sectional shape of a cone is represented by a Fourier series defining perturbations from the basic shape. The nonlinear equations of motion are perturbed from the circular (elliptic) cone case in a similar manner, resulting in approximate expressions for the flowfield when higher-order terms are neglected. The detailed procedure is described in Ref. 6 and summarized in Ref. 4. Performance predictions for waveriders based on these approximations, indicating the general effects of the geometrical and flight parameters, were given by Rasmussen[6] and Jischke.[4] Measurements of force, moment, and surface pressure conducted by Rasmussen et al.[7] and Jischke et al.[8] do not show very good quantitative agreement at the large eccentricity and inclination angle, but qualitative trends are correctly predicted.

Kim[9] investigated the lift and drag relations for an arbitrary conical waverider shape. This elegant approach, which does not invoke any hypersonic assumptions, shows that the lift and drag depend only on the flow in the shock layer base plane. Kim, Rasmussen, and Juschke[10] provided some interesting insight into the underlying principles. They suggest the application of the calculus of variations to determine optimum shapes subject to constraints on volume, lift, or other parameters.

A significant aspect of waverider design is the use of the attached shock at the nose. A blunt-nosed vehicle has a bow shock wave whose strength decays rapidly with downstream distance. The shock is detached and, at an angle of attack, a diverging crossflow is unavoidable. Alternatively, the waverider configuration allows for an attached shock wave that can prevent crossflow.

The aerodynamic characteristics and performance of waveriders can often be predicted quite well by inviscid analysis, especially in the case of inversely designed waveriders, which are derived by fitting known inviscid flowfields. Inviscid analysis can be divided into two groups: 1) purely analytical treatments that yield closed-form solutions to flowfield parameters such as pressure distribution and lift, and 2) the very recent numerical simulation of the inviscid full potential[11] or Euler[12-14] equations. These approaches are useful in their own right; however, the ultimate selection of desirable configurations is significantly influenced by viscous effects, the most obvious being friction drag and aerodynamic heating. As indicated previously,[10] configurations optimized by inviscid analysis are likely to have very large surface areas and, hence, large wetted areas. Viscosity also results in boundary-layer growth

Received Feb. 4, 1991; revision received Aug. 21, 1991; accepted for publication Sept. 6, 1991. 

*Graduate Student, Department of Mechanical and Aerospace Engineering and Engineering Mechanics.
†Associate Professor, Department of Mechanical and Aerospace Engineering and Engineering Mechanics.
‡Professor, Department of Mechanical and Aerospace Engineering.

that displaces the flowfield from the physical boundaries of the vehicle. This displacement effect does have some influence on the performance of waveriders, especially at high altitude (i.e., low Reynolds number). When the boundary-layer displacement is large, the shock wave geometry differs from its design condition, and, as a result, the pressure distributions are also perturbed. In principle, it is sometimes possible to compensate for boundary-layer displacement in waverider design. Therefore, it is necessary to know these effects accurately by solving the whole set of viscous flow equations directly.

Moreover, during vehicle maneuvering, certain viscous flow complications, such as shock-boundary-layer interactions, leading-edge flows, wake flows, and other flows that involve strong viscous-inviscid interactions resulting in large separated flow regions, might occur. Obviously, it is not possible to obtain accurate information on the flowfield using the simplified inviscid flow equations. An attempt to include viscous effects by coupling of viscous drag effects with inviscid analytical methods along with configuration optimization has been made by Bowcutt et al.[15] However, solution of the complete set of Navier-Stokes equations will shed much more light on the complex phenomena associated with the waverider flowfield. In recognition of the fact that, to the best of our knowledge, the studies conducted so far on waveriders by the various investigators have not attempted simulation of the Navier-Stokes equations, the present work for the detailed analysis by means of the cited numerical algorithms will yield important information to the designer regarding forces, aerodynamic heating, propulsion integration, and stability of the aircraft. The present study has been conceived with the purpose of gaining a detailed understanding of waverider characteristics by considering the viscous effects in more depth than was attempted before.[15] The numerical simulation of the full Navier-Stokes equations was the logical tool that we chose for this purpose.

## II. Governing Equations and Numerical Algorithm

The equations to be satisfied in the physical field are the continuity, momentum, and energy equations as given by Eqs. (1-3). The dependent variables are density $\rho$, velocity components $u,v,w$, and total energy per unit volume $E_t$.

Continuity equation:

$$\frac{\partial \rho}{\partial t} + \nabla \cdot (\rho V) = 0 \tag{1}$$

Momentum equation:

$$\frac{\partial \rho V}{\partial t} + \nabla \cdot (\rho VV + p\delta_{ij} - \tau_{ij}) = 0 \tag{2}$$

Energy equation:

$$\frac{\partial E_t}{\partial t} + \nabla \cdot [E_t V + (p\delta_{ij} - \tau_{ij}) \cdot V - k \nabla T] = 0 \tag{3}$$

A calorically perfect fluid with constant specific heat was assumed. Fourier's law of heat conduction was used to describe the heat transfer rate in the fluid. The total energy is defined in Eq. (4), where $e$ denotes the specific internal energy:

$$E_t = \rho(e + \tfrac{1}{2}|V|^2) \tag{4}$$

The viscous stresses $\tau_{ij}$ are given in Eq. (5), where the viscosity $\mu$ is described by Sutherland's law as a function of temperature:

$$\tau_{ij} = \left[ \mu\left(\frac{\partial u_i}{\partial x_j} + \frac{\partial u_j}{\partial x_i}\right) + \lambda\delta_{ij}\frac{\partial u_k}{\partial x_k} \right] \tag{5}$$

An additional equation for compressible flow is required; this is called an equation of state (6):

$$p = (\gamma - 1)\rho e \tag{6}$$

These equations are essentially of a convective nature and, hence, directionally biased. Therefore, the physical properties of the convective terms and the pressure terms were introduced in the discretization process employed in the present method to obtain higher resolution and favorable stability. The solution was achieved using the implicit, finite-volume, upwind algorithm described in Refs. 16-20. The Navier-Stokes equations are solved in conservation law form under the generalized coordinate transformation, $x^i = [\xi,\eta,\zeta]^t$ with respect to $x_i = [x,y,z]^t$. The equations can be rewritten in integral form for a bounded finite volume $\Omega$ with its corresponding cell surface boundary $\partial\Omega$,

$$\frac{\partial}{\partial t}\int_\Omega Q \, dv + \oint_{\partial\Omega} [\bar{f}(\hat{n}) - \bar{v}(\hat{n})] \, ds = 0 \tag{7}$$

Here, $Q$ is the vector of conserved variables for mass, momentum, and energy. The vectors $\bar{f}$ and $\bar{v}$ are the directed inviscid and viscous fluxes, respectively, with respect to the outward cell surface normal $\hat{n}$. The approximate Riemann's solver of Roe,[21,22] is used for the numerical representation of the inviscid fluxes. The state variables are obtained by using MUSCL (monotone upstream-centered schemes for conservation laws) interpolation of the primitive variables $q = [\rho,u,v,w,p]^t$. Second-order central differencing is used for viscous fluxes, and the thin-layer approximation is made for each direction.

The no-slip and impermeable wall boundary conditions, zero normal pressure gradient at the wall, and the adiabatic wall boundary conditions were imposed in the present calculations. First-order extrapolation of the primitive variables were used along the downstream boundary. The outer boundary conditions were specified as either the freestream flow property or the locally one-dimensional inflow/outflow characteristic solutions. The initial flow conditions were specified as uniform freestream flow.

## III. Grid Generation

The geometric configuration analyzed by numerical calculation was one of those tested by Rasmussen et al.[7] and Jischke et al.,[8] as shown in Fig. 1. Because of its geometric simplicity and favorable aerodynamic characteristics, it is selected for the present study.

Algebraic systems, in which the coordinates are determined by interpolation (using functions), and partial differential equations, were used in this study to generate the grid described in the following by taking advantage of the specific geometry and flowfield. Using GRAPE2D,[23] the coordinates in the last $JK$ plane (Fig. 2) are generated by solving the

model dimensions, *in*

| L | W | T | $A_b$, $in^2$ |
|---|---|---|---|
| 23.62 | 21.50 | 7.11 | 75.83 |

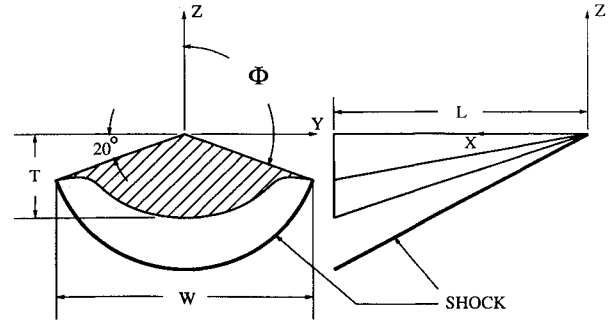


**Fig. 1 Elliptic-cone waverider configuration.**

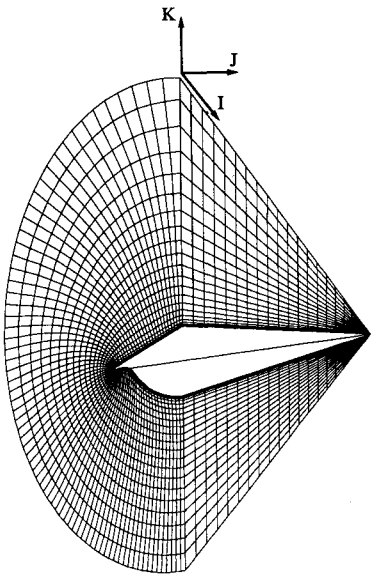


Fig. 2 Grid topology.

two-dimensional Poisson's equation. In the present study, the smallest distance of the first grid away from the body surface in the normal direction was chosen to have a constant value for the last *JK* plane everywhere around the circumference, and it varied in the range 0.00254–0.00127 cm (0.001–0.0005 in.). The outer boundary reaches up to 50.8–63.5 cm (20–25 in.) away from the surface. The remaining *JK* planes, then, can be generated by translating this two-dimensional grid at finite intervals with perspective projection up to the nose. The entire grid topology is shown in Fig. 2, where *I* is the streamwise direction, *J* the circumferential direction, and *K* the normal direction, with $41 \times 74 \times 51$ grid points in total.

## IV. Results and Discussion

### A. Original Experiments

The model, shown in Fig. 1, was derived from the flow past an elliptic cone at zero angle of attack and is referred to as the elliptic-cone waverider. The shape of the curved surface, which is a conical streamsurface for the elliptic-cone flow, is given approximately by

$$\frac{\theta}{\delta} = 1 - 0.1\cos 2\phi + (0.39 + 0.1\cos 2\phi)\left[\frac{\tan(\pi - \phi)}{2.75}\right]^{7.69} \quad (8)$$

where $\delta$ is the semivertex angle of the basic cone, $\theta$ the polar angle (measured from the $X$ axis), and $\phi$ the azimuthal angle. The basic-cone angle for this model was selected as 18.62 deg. The design Mach number for this waverider model is equal to 4. Thus, for the design condition, the shock will be attached to the waverider lip at $\phi = \pm 110$ deg. Experiments[7,8] were done in the Mach number range 3–5 and the unit Reynolds number range $3.28–6.56 \times 10^6$/m. Angle of attack and side-slip angle were varied in the range $\pm 20$ deg. Lift and drag data and surface pressure distributions are available for this configuration. Schlieren and surface oil flow visualization data were also obtained.

General results obtained from the experiments are described as follows. The maximum lift-to-drag ratios of the waverider are found to be 2.5 times greater than that of the comparable simple elliptic cone. Normal force and rolling moment coefficients, along with the lift-to-drag ratios, are found to decrease for the waveriders as the Mach number increases. The force, moment, and surface pressure data corroborate the basic conical flow assumption and substantiate the accuracy of the perturbation theory that underlies the waverider configuration design for the on-design conditions. However, the data also show deviations from analytic solutions at off-design conditions; i.e., at angle of attack/side-slip and Mach number different from the design values. The schlieren data give the shock wave positions, and the oil flow studies suggest that the flows were conical and laminar over the entire range of testing conditions.

### B. Model Problems

Before proceeding with the investigation of waveriders, a series of model problems were considered to validate the present numerical techniques, results of which are summarized in Table 1. For the first two cases for the flat plate, the grid was uniform in the streamwise direction and stretched in the cross-stream direction. The solutions of these model problems confirm that the numerical procedure does perform as expected. The numerical investigation of waveriders is discussed in the following sections.

### C. Waverider at Zero Angle of Attack

The first case of the present numerical investigation is to calculate the waverider flowfield at zero angle of attack. It is very important to calculate the flow at this condition since this

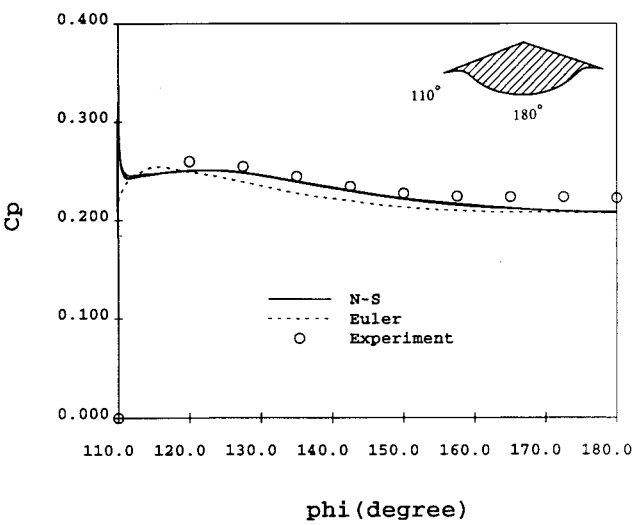


**Fig. 3 Pressure coefficient on lower surface, $x = 15.7$ in. for experimental data (180 deg corresponds to the centerline, 110 deg to the tip): $M_\infty = 4.0$; $Re = 2$ m/ft; $\alpha = 0.0$ deg.**

**Table 1 Model problems**

| Case | $Re$ | $M_\infty$ | Grid size | Comments |
|---|---|---|---|---|
| Flat plate | | | | |
| Subsonic | $10^4$ | 0.5 | $76 \times 51$ | Excellent agreement with Blasius solution |
| Supersonic | $1 \times 10^6$ | 4.0 | $101 \times 101$ | Excellent agreement with Van Driest[24] |
| Shock boundary-layer interaction | $2.96 \times 10^5$ | 2.0 | $96 \times 93$ | Good agreement with experiments[25] and other CFD simulations |

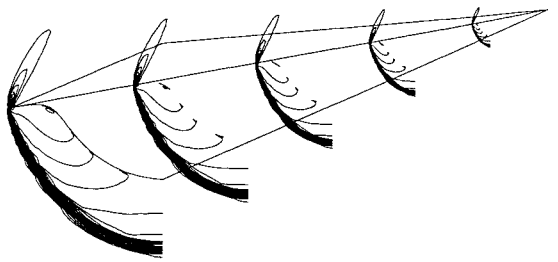

**Fig. 4 Pressure contours at several cross planes: $M_\infty = 4.0$; $Re = 2$ m/ft; $\alpha = 0.0$ deg.**

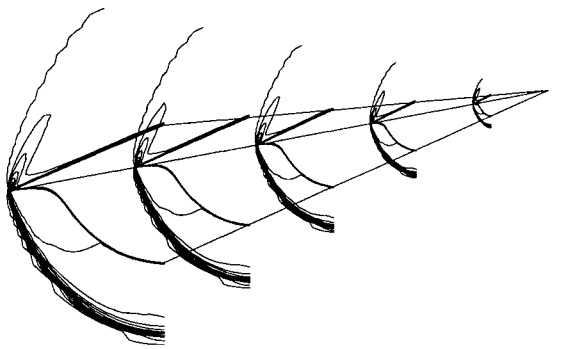

**Fig. 5 Mach number contours at several cross planes: $M_\infty = 4.0$; $Re = 2$ m/ft; $\alpha = 0.0$ deg.**

is the baseline case used to design the geometric profile of the model. Two different numerical approaches, quasi-three-dimensional [$2 \times 99 \times 61$] (Euler solution with two $JK$ planes only) and full three-dimensional [$41 \times 74 \times 51$], have been considered.

All the results presented here are for steady flow and for the forebody only, 60 cm (23.62 in.) in length. Computations are carried out at zero angle of attack, Mach number = 4.0, and Reynolds number = $6.56 \times 10^6$/m. These are the same conditions as the ones used in the experiments. In all of the computed cases, the flow was considered laminar, as observed from the experiments, and accordingly, no turbulence modeling was used.

The computed pressure coefficients (circumferential distribution) at several axial stations are shown as the solid lines (overlaying) in Fig. 3, together with the experimental measurements shown as full circles. An additional inviscid pressure distribution obtained with the quasi-three-dimensional flow calculation with the viscous terms and no-slip boundary condition removed and the conical inflow/outflow boundary conditions introduced is also shown in this figure. It can be seen from the figure that the pressure coefficient plots from these viscous solutions at different streamwise stations are almost identical to each other. Therefore, this figure numerically proves the conical flow feature of the flowfield. When comparing the two different types of numerical results, we can observe that the viscous/inviscid interaction effects are not strong in this specific case, since the viscous effects are confined to a well-behaved laminar boundary layer.

Computed pressure and Mach number contours at several cross planes along the entire body are shown in Figs. 4 and 5. A two-dimensional plot of the pressure contours at a particular station, $x = 39.88$ cm (15.7 in.), is shown in Fig. 6. The general pattern of these contours shows that the shock features, in terms of the relative contour levels and gradients, are well captured. It is seen that the shock is slightly away from the wingtip instead of being exactly attached at the leading edge; this has probably caused a flow relief effect. Therefore, the pressure on the upper surface is no longer the same as the freestream pressure; but, as seen from the printed results, it is slightly more than that value. At the same time, the strength of the nonattached shock appears to be weaker than that of the

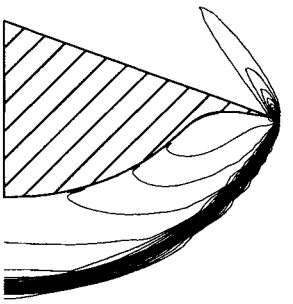

**Fig. 6 Two-dimensional pressure contours at $x = 15.7$ in.: $M_\infty = 4.0$; $Re = 2$ m/ft; $\alpha = 0.0$ deg.**

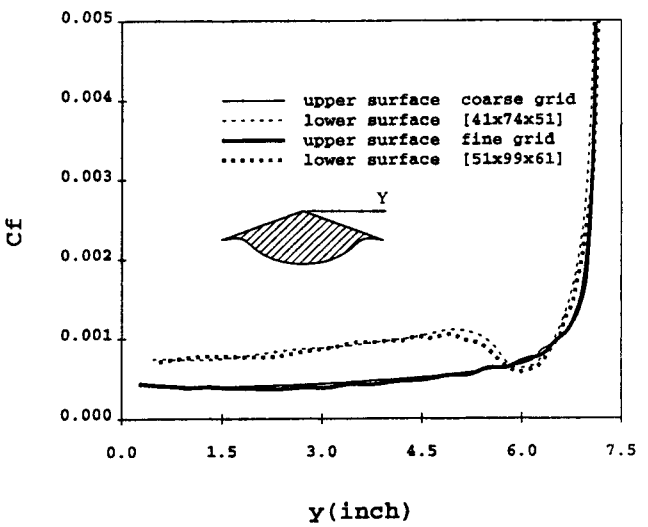


**Fig. 7 Circumferential variation of skin friction coefficient at $x = 15.7$ in.: $M_\infty = 4.0$; $Re = 2$ m/ft; $\alpha = 0.0$ deg (thick lines represent results using finer grid).**

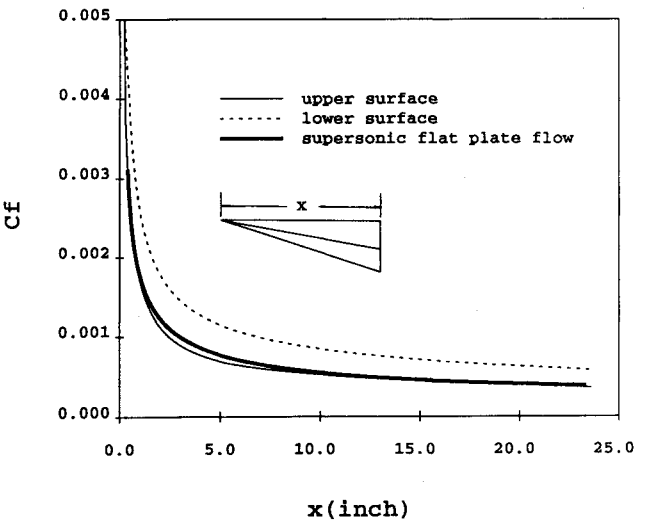


**Fig. 8 Axial variation of skin friction coefficient: $M_\infty = 4.0$; $Re = 2$ m/ft; $\alpha = 0.0$ deg (thick line represents numerical values of supersonic flat plate flow).**

attached shock, causing the pressure across the shock not to be as high as the design value.

Results from other studies[11,12] also show the shock being detached at the design condition. Yoon and Rasmussen[12] explained this as being the result of using the approximate hypersonic small disturbance theory (HSDT) to derive the waverider shape. These authors argue that an attached shock can be

Table 2 Waverider aerodynamic parameters

| $\alpha$, deg | $C_L$ | $\bar{c}_f$ | $C_D$ | $C_L/C_D$ |
|---|---|---|---|---|
| 0 | 0.76317 | 0.00737 | 0.23471 | 3.25154 |
| 5 | 1.19060 | 0.00672 | 0.44035 | 2.70373 |

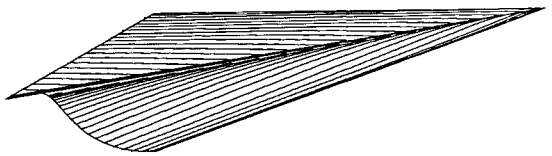

Fig. 9 Particle traces on surface: $M_\infty = 4.0$; $Re = 2$ m/ft; $\alpha = 0.0$ deg.

expected only if the waverider geometry is based on the exact solution to the corresponding elliptic-cone flow, and the solution to the flow past such a waverider is also exact.

The numerical results, in fact, give much more information than the experiments. The circumferential variation of the skin friction coefficient at the axial station, $x = 39.88$ cm (15.7 in.), are shown in Fig. 7, and those along the axial direction in the symmetry plane are shown in Fig. 8. The thick lines in Fig. 7 present the results based on finer grids ($51 \times 99 \times 61$). It is evident from these plots that the numerical solution based on the [$41 \times 74 \times 51$] grid is, for all practical purposes, grid independent. The thick line in Fig. 8 presents the values of the skin friction coefficient obtained by numerical calculation of the supersonic flat plate flow at the same $Re$ and $M_\infty$ values and is seen to compare well with the waverider upper surface, as expected. The average (length-weighted) skin friction values on the upper surface and the lower surface centerlines have been evaluated from the results of Fig. 8 as 0.00059158 and 0.00094428, respectively. Since the calculations are at the design condition, the freestream is basically aligned with the upper surface. Van Driest's[24] calculations for a flat plate gave $\bar{c}_f\sqrt{Re_\infty} = 1.15$, where $\bar{c}_f$ is the average value of the skin friction coefficient. By comparison, our computations for the upper surface give $\bar{c}_f\sqrt{Re_\infty} = 1.17$.

In the work of Kim et al.,[14] they estimated an empirical value for the average skin friction coefficient, which is based on laminar flow over a flat plate. For laminar flat plate flow, $\bar{c}_f$ is approximated by $1.328\, f(M_\infty)/\sqrt{Re}$, where $Re$ is the freestream Reynolds number based on length, and $f(M_\infty)$, a function of Mach number, is somewhat less than unity. They made an analysis of the effect of friction drag on lift-to-drag ratio. They used the expression

$$D = D_w + qS_w\bar{c}_f$$

where $D_w$ is the wave drag, $S_w$ the wetted area of the body, defined in Ref. 9, and $q$ the freestream dynamic pressure. Following this model, the present numerical results show that the lift and forebody drag coefficients, obtained by integrating the pressure and shear stresses at each surface grid point, are as given in Table 2. The waverider base area was used as the reference area for calculating these coefficients. It is to be noted that the $C_D$ values in Table 2 do not include the base pressure drag. The skin friction drag contribution for the zero angle-of-attack case is about 3.4% of the total drag.

Computed surface particle traces are shown in Fig. 9. Particle traces are computed by assuming that the flow is steady and by releasing a particle at each grid point in the first layer of points above the body. The particles move with the local fluid velocity, but are constrained to stay just above the body; that is, the normal velocity component is set to be zero in the time integration. Such computed surface particle traces are the numerical equivalent of the streamlines in steady flow. This figure appears to substantiate the design concept, discussed at the beginning of the paper, which prevents diverging crossflow on the lifting surface of the waverider to yield higher lift due to higher pressure.

Interestingly, when comparing the numerical and available experimental results, some discrepancy can be seen. Qualitatively speaking, numerical results and experimental results have the same trend as can be seen from Fig. 3; however, they reveal up to a 10% difference in the pressure coefficient, the experimental values being higher than the numerical results. As mentioned previously, this is a baseline case used to evaluate the configuration and, therefore, involves questions about the design concept of waveriders. Therefore, it is worthwhile to put forth more effort to study the possible causes behind the observed disagreement.

A distinct possibility for this discrepancy in $C_p$ values is related to the fact that these values are very sensitive to the shock position for this type of problem. Therefore, in addition to the necessity to employ high-resolution shock capturing numerical schemes (such as the present one), it is essential that one specify inputs to the computer program that correspond to the actual flow situation existing in the experimental setup. Because of the author's inability to explain the discrepancy of Fig. 3, we contacted one of the authors[26] of the experimental study who suggested to us that the model might have, in fact, been at a slight angle of attack. An estimate of the angle-of-attack misalignment was made using the analysis given by Ras-

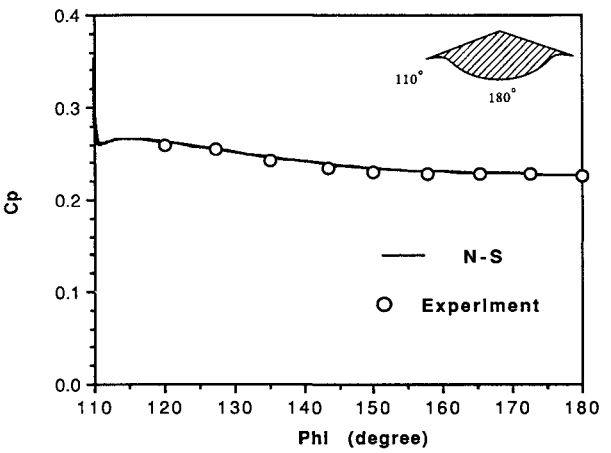


Fig. 10 Pressure coefficient on lower surface, $x = 15.7$ in. for experimental data and modified angle of attack (180 deg corresponds to the centerline, 110 deg to the tip): $M_\infty = 4.0$; $Re = 2$ m/ft; $\alpha = 0.9$ deg.

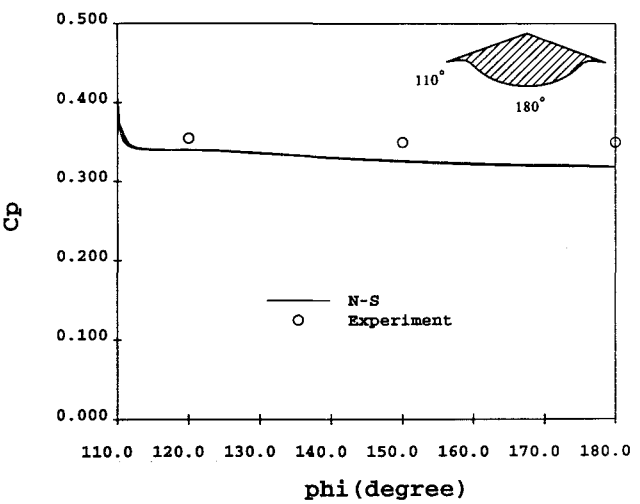


Fig. 11 Pressure coefficient on lower surface, $x = 15.7$ in. for experimental data (180 deg corresponds to the centerline, 110 deg to the tip): $M_\infty = 4.0$; $Re = 2$ m/ft; $\alpha = 5.0$ deg.

mussen.[6] The pressure coefficient in the shock layer for slender cones at high Mach numbers is given quite accurately by

$$\frac{C_p(\theta)}{\delta^2} = 1 + \frac{\sigma^2}{\sigma^2 - 1}\left[1 + \ell n\left(\frac{\beta^2}{\theta^2}\right) - \frac{\delta^2}{\theta^2}\right]$$

where $\theta$ is the angle from cone axis $\delta \le \theta \le \beta$, $\sigma = \{[(\gamma + 1)/2] + 1/K_\delta^2\}^{1/2}$, $\gamma$ is the ratio of specific heats, and $K_\delta = M_\infty \delta$. In turn, our estimate suggested that $\alpha = +0.9$ deg would bring coincidence to the experimental and computational results. The $C_p$ results of this slight variation in angle of attack are shown in Fig. 10.

### D. Waverider at Angle of Attack

The following case has the same Mach number and Reynolds number as the previous zero angle-of-attack case, but the angle of attack is increased to 5 deg. Portions of the numerical results are shown in Figs. 11–13. From Fig. 11, we can see that the conical flow feature with respect to the pressure distribution is still preserved for the $\alpha = 5$ deg case, since the azimuthal pressure coefficient results at different streamwise stations are invariant with axial location. However, comparison with experimental data, the circles in the figure, shows much more discrepancy than the zero angle-of-attack case. Computed pressure and Mach number contours at several cross planes along the entire body length are shown in Figs. 12 and 13. A two-dimensional plot of the pressure contours at a particular station, $x = 39.88$ cm (15.7 in.), is shown in Fig. 14. As with the zero angle-of-attack case, these contours also show the well-captured shock features in terms of the relative contour levels. However, it is seen that the shock is much more detached from the wingtip compared to the zero angle-of-attack case. This result is most certainly caused by the larger incident angle inducing a shock cone of higher angle, which in turn leads to the higher pressure on the lower surface. We can also observe that the pressure and Mach number contours are more closely packed than in the zero angle-of-attack case; this feature probably reveals the higher shock strength in the $\alpha = 5$-deg case.

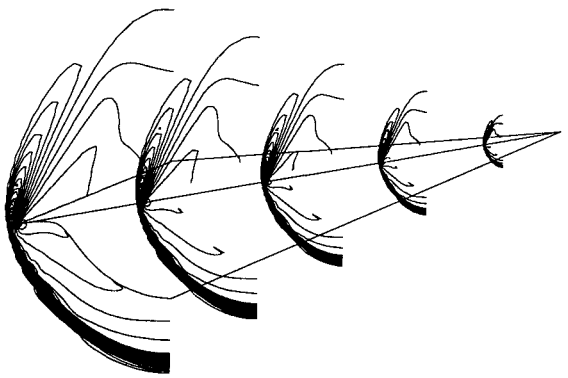

**Fig. 12 Pressure contours at several cross planes: $M_\infty = 4.0$; $Re = 2$ m/ft; $\alpha = 5.0$ deg.**

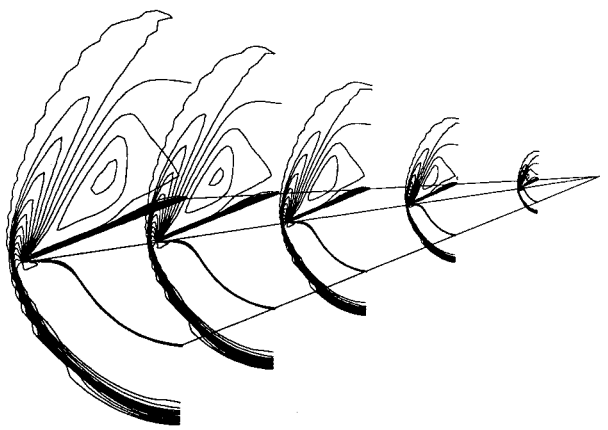

**Fig. 13 Mach number contours at several cross planes: $M_\infty = 4.0$; $Re = 2$ m/ft; $\alpha = 5.0$ deg.**

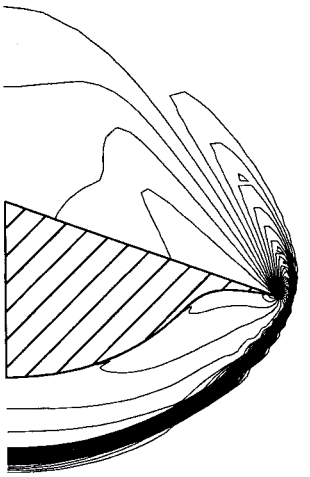

**Fig. 14 Two-dimensional pressure contours at $x = 15.7$ in.: $M_\infty = 4.0$; $Re = 2$ m/ft; $\alpha = 5.0$ deg.**

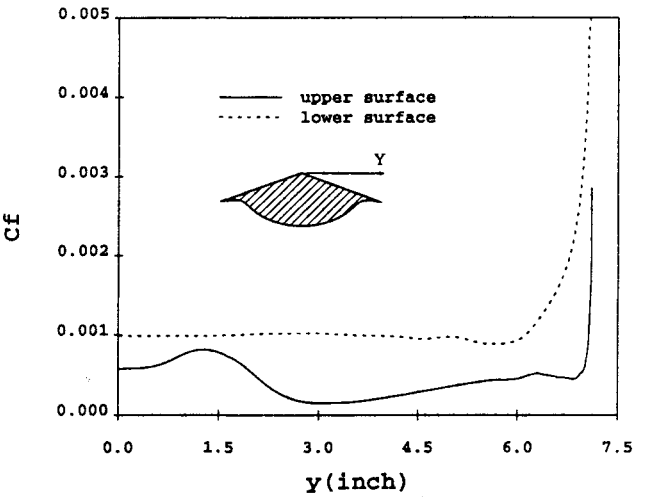


**Fig. 15 Circumferential variation of skin friction coefficient at $x = 15.7$ in.: $M_\infty = 4.0$; $Re = 2$ m/ft; $\alpha = 5.0$ deg.**

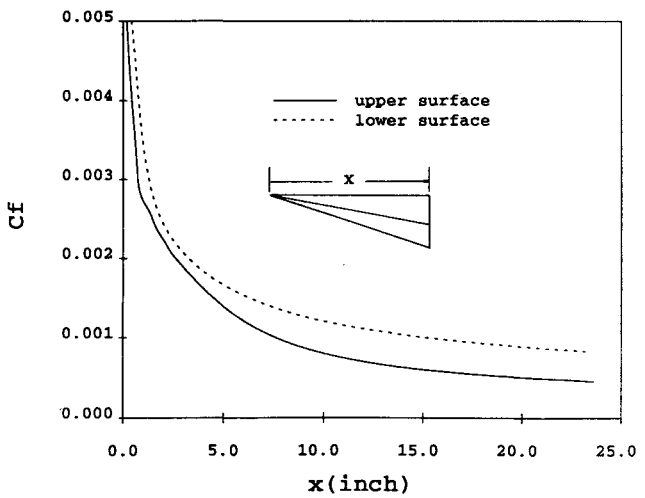


**Fig. 16 Axial variation of centerline skin friction coefficient: $M_\infty = 4.0$; $Re = 2$ m/ft; $\alpha = 5.0$ deg.**

The computed laminar skin friction coefficients are given in Figs. 15 and 16. They show that the skin friction coefficients

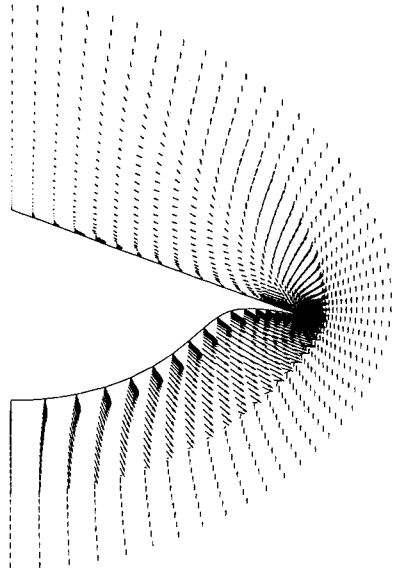

**Fig. 17 Velocity vectors of cross flow at $x = 15.7$ in.: $M_\infty = 4.0$; $Re = 2$ m/ft; $\alpha = 5.0$ deg.**

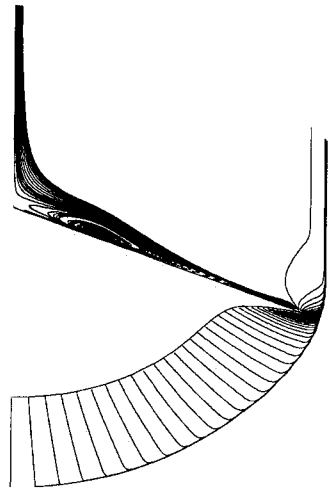

**Fig. 18 Particle traces of cross flow at $x = 15.7$ in.: $M_\infty = 4.0$; $Re = 2$ m/ft; $\alpha = 5.0$ deg.**

generally increased on the windward surface and decreased on the leeward surface due to the angle-of-attack effect. Another interesting aspect of this case is that the skin friction coefficients on the upper surface at $x = 39.88$ cm (15.7 in.) (Fig. 15) show a wave-type variation, which was not present in the zero angle-of-attack case. In an effort to explain this observation, the crossflow velocity vectors at the same station, $x = 39.88$ cm (15.7 in.), are shown in Fig. 17; the particle traces of the same crossflow are also shown in Fig. 18. These two plots reveal the appearance of two vortices on each half of the leeward side much like those on a delta wing at angle of attack. Of these two, the vortex near the tip is seen to be much smaller compared to the one near the ridge. The undulations in the skin friction variation also correspond in size and location to these vortices. At the same time, the vortex that existed on the windward side at zero angle of attack has attenuated in strength as indicated by the smaller dip in the lower surface skin friction coefficient toward the tip. This is probably due to the considerable crossflow taking place from the lower to the upper surface in this 5-deg angle-of-attack case caused by the shock not being attached to the leading edge any more. Thus, we see that even at this moderate angle of attack, the flowfield has become quite complex. The lift and drag values for this case are shown in Table 2. The skin friction drag contribution for the 5-deg angle-of-attack case is about 1.526% of the total drag. The lift-to-drag ratio has decreased for this case by about 17% from the zero angle-of-attack case.

Higher angle-of-attack cases and off-design Mach number cases will be considered as a continuation of this investigation.

## V. Conclusions

The three-dimensional, laminar flowfield associated with waveriders has been analyzed by successful simulation of the Navier-Stokes equations. All of the computations were obtained using CFL3D, developed by NASA Langley Research Center, based on modern numerical techniques for time-dependent Navier-Stokes equations. The solutions of the model problems confirm that the numerical procedure does perform as expected and the results agree very well with the numerical studies using other algorithms. The numerical results of waveriders at zero angle of attack also have been validated by comparing with flat plate flow.

The Navier-Stokes simulation of the waverider flowfield resulting in favorable aerodynamic characteristics (i.e., high lift/drag ratio) shows that waverider shapes are viable configurations for high-speed aircraft. The aerodynamic performance of the waverider stays within acceptable limits at low angles of attack. However, even at small (5-deg) angles of attack, the flowfield shows the formation of vortices as well as the detachment of the shock from the leading edge. Thus, we see that the flowfield has become quite complex. Viscous effects will be critical for proper consideration of aeropropulsion integration, aerothermal heating, and separated flow. Until realistic waverider configurations are thoroughly studied at off-design conditions, they cannot be seriously considered as practical designs. With the advances in computational fluid dynamics, we can analyze these flows in detail.

Important information can be obtained by extending the present study to include turbulent boundary-layer and wake calculations with appropriate turbulence modeling, heat transfer calculations, and characteristics of the flowfield at engine inlet. Future studies must also include a range of off-design conditions in order to establish the versatility of waveriders. The authors are continuing along these lines with the goal of establishing the necessary data base for using waverider shapes for aircraft design.

## Acknowledgments

The authors thank the University of Illinois, National Center for Supercomputer Applications, for a grant for the use of the Cray-2 computer, on which the three-dimensional runs have been made. The authors also gratefully acknowledge financial support from the University of Missouri Weldon Spring Endowment in the form of an intercampus research grant for conducting this study. The numerical results are based on the computer program CFL3D. The authors thank Jim Thomas, Sherrie Krist, and Pam Richardson, NASA Langley Research Center, for making the program available.

We also extend our thanks to Martin Jischke, president, Iowa State University (formerly, chancellor, University of Missouri-Rolla), for his interest and input during the course of this work. The grid system has been generated by extending the grid generation procedure use in the program GRAPE, written at the NASA Ames Research Center.

## References

[1]Eggers, A. J., Resnikoff, M. M., and Dennis, D. H., "Bodies of Revolution Having Minimum Drag," NACA RM A55I05, 1956.

[2]Hemsch, M. J., and Nielsen, J. N. (eds.), *Tactical Missile Aerodynamics,* Vol. 104, Progress in Astronautics and Aeronautics, AIAA, New York, 1986, pp. 198–242.

[3]Maikapar, G. I., "Bodies Formed by the Stream Surfaces of Conical Flow," *Mekhanika Zhidkostii Gaza,* Vol. 1, No. 1, 1966, pp. 126, 127.

[4]Jischke, M. C., "Supersonic Flow past Conical Bodies with Nearly Circular Cross Section," *AIAA Journal,* Vol. 19, No. 2, 1981, pp. 242–245.

[5]Doty, R. T., and Rasmussen, M. L., "Approximation for Hypersonic Flow Past and Inclined Cone," *AIAA Journal,* Vol. 11, No. 9, 1973, pp. 1310–1315.

[6]Rasmussen, M. L., "Waverider Configurations Derived from Inclined Circular and Elliptic Cones," *Journal of Spacecraft and Rockets,* Vol. 17, No. 6, 1980, pp. 537–545.

[7]Rasmussen, M. L., Jischke, M. C., and Daniel, D. C., "Experimental Forces and Moments on Cone-Derived Waveriders for $M = 3$–5," *Journal of Spacecraft and Rockets,* Vol. 19, No. 6, 1982, pp. 592–598.

[8]Jischke, M. C., Rasmussen, M. L., and Daniel, D. C., "Experimental Surface Pressures and Cone-Derived Waveriders for $M = 3$–5," *Journal of Spacecraft and Rockets,* Vol. 20, No. 6, 1983, pp. 539–545.

[9]Kim, B. S., "Optimization of Waverider Configurations Generated from Non-Axisymmetric Flows past a Nearly Circular Cone," Ph.D. Dissertation, Univ. of Oklahoma, Norman, OK, 1984.

[10]Kim, B. S., Rasmussen, M. L., and Jischke, M. C., "Optimization of Waverider Configurations Generated from Axisymmetric Conical Flows," *Journal of Spacecraft,* Vol. 20, No. 5, 1983, pp. 461–469.

[11]Jones, K. M., "Application of a Supersonic Full Potential Method for Analysis of Waverider Configurations," NASA TP 2608, Sept. 1986.

[12]Jones, K. D., and Dougherty, F. C., "Computational Simulation of Flows about Hypersonic Geometries with Sharp Leading Edges," AIAA Paper 90-3065, Aug. 1990.

[13]Yoon, B. H., and Rasmussen, M. L., "Computational Analysis of Hypersonic Flows past Elliptic-Cone Waveriders," Univ. of Oklahoma, Research Rept. OU-AME-91-2, Norman, OK, Jan. 1991.

[14]Long, L. N., "Off-Design Performance of Hypersonic Waveriders," *Journal of Aircraft,* Vol. 27, No. 7, 1990, pp. 639–646.

[15]Bowcutt, K. G., Anderson, J. D., and Capriotti, D., "Viscous Optimized Hypersonic Waveriders," AIAA Paper 87-0272, Jan. 1987.

[16]Anderson, W. K., Thomas, J. L., and Van Leer, B., "Comparison of Finite Volume Flux Vector Splittings for the Euler Equations," *AIAA Journal,* Vol. 24, No. 9, 1986, pp. 1453–1460.

[17]Thomas, J. L., and Walters, R. W., "Upwind Relaxation Algorithms for the Navier-Stokes Equations," *AIAA Journal,* Vol. 25, No. 4, 1987, pp. 527–534.

[18]Van Leer, B., Thomas, J. L., Roe, P. L., and Newsome, R. W., "A Comparison of Numerical Flux Formulas for Euler and Navier-Stokes Equations," AIAA Paper 87-1104, June 1987.

[19]Thomas, J. L., Taylor, S. L., and Anderson, W. K., "Navier-Stokes Equations Computations of Vortical Flows over Low Aspect Ratio Wings," AIAA Paper 87-0207, Jan. 1987.

[20]Vatsa, V. N., Thomas, J. L., and Wedan, B. W., "Navier-Stokes Equations Computations of Prolate Spheroids at Angle of Attack," AIAA Paper 87-2627, Aug. 1987.

[21]Roe, P. L., "The Use of the Riemann Problem in Finite Difference Schemes," *Lecture Notes in Physics,* Vol. 141, Springer-Verlag, Berlin, 1981, pp. 354–359.

[22]Roe, P. L., "Approximate Riemann Solvers, Parameter Vectors and Difference Schemes," *Journal of Computational Physics,* Vol. 43, 1981, pp. 357–372.

[23]Sorenson, R. L., "A Computer Program to Generate Two-Dimensional Grids About Airfoils and Other Shapes by the Use of Poisson's Equation," NASA TM 81198, May 1980.

[24]Van Driest, E. R., "Investigation of Laminar Boundary Layer in Compressible Fluids Using the Crocco Method," NACA TN 2597, Jan. 1952.

[25]Hakkinen, R. J., Greber, I., Trilling, L., and Arbarbanel, S. S., "The Interaction of an Oblique Shock Wave with a Laminar Boundary Layer," NACA Memo-2-18-59W, March 1959.

[26]Jischke, M. C., private communication, Dec. 1990.